

Morphological Control of Nanoporous Copper Formed from Conversion Reaction Synthesis

Shijie Feng, Victoria Petrova, Adam A. Corrao, Shen Wang, Kesong Yang, Peter G. Khalifah, and Ping Liu*



Cite This: *J. Phys. Chem. C* 2022, 126, 14878–14885



Read Online

ACCESS |



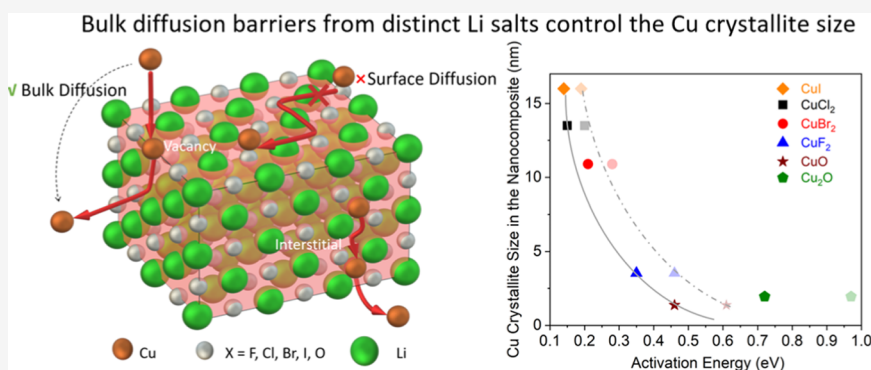
Metrics & More



Article Recommendations



Supporting Information



ABSTRACT: The pore architecture of nanoporous copper (NP-Cu) plays a vital role in its technological applications. The synthesis of NP-Cu by the conversion reaction has been reported, where an ionic Cu precursor (salt or oxide) is chemically reduced with *n*-butyllithium to form a Cu metal nanocomposite, from which the Li-containing product is removed to form NP-Cu. Anions in the Cu compound precursors significantly affect the size of Cu in the nanocomposite due to the effect of lithium salt on Cu diffusion. Thermal annealing of the nanocomposites reveals that the activation energy for diffusion correlates with the melting point of the lithium salt, which is used as a proxy for their tendencies of forming defects, indicating that Cu diffusion takes place through the bulk phase of the salt rather than the Cu/salt interfaces. This experimentally observed behavior is consistent with the results from density functional theory calculations. Further, doping the lithium salt with Mg²⁺ increases the defect concentration and facilitates enhanced Cu diffusion. The choice of anion in the Cu salt precursor thus provides an effective tool to enable control of the nanoscale size of Cu and the resultant NP porosity.

INTRODUCTION

Nanoporous copper (NP-Cu) has a broad range of applications such as plasmonic materials,^{1–3} catalysts,^{4–6,12,13} energy storage materials,⁷ actuators,⁸ bonding materials,^{9–11} and among others. These applications take advantage of the NP-Cu's 3D porous architecture, high surface area, good electrical conductivity, and lower cost than Ag and Au alternatives. The morphology of the microstructure, including the size and crystallinity of the Cu and the pore structure can dramatically affect its performance. For example, it has been reported that there is an optimal nanopore size for enhancing the surface enhancement Raman spectroscopy effects of NP-Cu.^{2,12,13} In addition, the pore size has been found to influence product selectivity in the CO₂ reduction reaction catalyzed by NP-Cu.^{5,6} Morphological control is essential to realize the full potential of NP-Cu in applications.

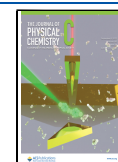
Conversion reaction synthesis (CRS) is a facile and scalable method to fabricate nanoporous metals.¹⁴ In a typical two-step CRS process, an ionic transition metal compound (e.g., CuCl₂) is first chemically reduced to a metal/lithium salt nano-

composite (e.g., Cu/LiCl) by *n*-butyllithium (*n*-BuLi, C₄H₉Li) dissolved in hexane. After conversion, a polar solvent such as methanol is used to remove the lithium-containing product (e.g., LiCl), leaving behind a nanoporous metal framework. Note that during the conversion step, CuCl₂, Cu, and LiCl have no solubility in hexane. The reaction is largely a solid–solid conversion process. Unlike the well-known dealloying process,¹⁵ the CRS approach allows for the synthesis of any nanoporous metal with an electrochemical potential higher than that of *n*-BuLi (1 V vs Li/Li⁺), thus providing access to a wide range of relevant metals. We have previously shown^{14,18} that the metal cation in the halide precursors plays an

Received: May 22, 2022

Revised: August 16, 2022

Published: August 23, 2022



important role in determining the feature size of nanoporous metal networks, largely due to the varying mobilities of the selected metal. For example, copper chloride (CuCl_2) was found to produce a larger crystallite size in the final nanoporous metal than iron chloride (FeCl_2) and cobalt chloride (CoCl_2). However, there is an as-yet unmet need to develop a method to control the size and architecture for a given metal. It has previously been observed that there are small differences in NP-Cu prepared with CuCl_2 and CuBr_2 precursors,¹⁴ suggesting that the anion choice may provide morphological control. In this work, a wide range of anions available with different sizes and chemical properties were investigated as precursors for the synthesis of NP-Cu, allowing us to observe large differences in the porosity of the resulting nanoporous metal and enabling us to investigate the salt properties that most directly control the product morphology.

The role of anions in influencing the NP-Cu structure can be both physical and chemical in nature. Lithium salts formed by different anions have significantly different molar volumes. A higher volume fraction of lithium salt may increase the required diffusion distance for Cu, thus limiting the size of the nanoparticles.¹⁴ In addition, the chemical interactions between metallic Cu and the anion in the lithium salt may influence the barrier heights associated with atom diffusion. It is possible that stronger bonding between Cu and the anion provided by the Li salts may hinder the Cu diffusion,^{16,17} also serving to limit the particle size. Motivated by these hypotheses, a systematic study of NP-Cu synthesized from different precursors was carried out to investigate the influence of the anion on the size of microstructural features in the nanocomposites produced through CRS reactions. Nanocomposites were synthesized from different Cu precursors and characterized, providing insights into the origin of the anion influence on feature sizes in NP-Cu.

EXPERIMENTAL METHOD

Nanocomposite Preparation and Thermal Annealing.

Unless otherwise stated, all commercial reagents and solvents were used as commercially purchased without additional purification. We have previously reported that metal/lithium salt nanocomposites are synthesized by reacting anhydrous precursors with *n*-butyllithium (1.6 M) in hexane.^{14,18} All synthesis procedures were carried out in an argon glovebox (≤ 10 ppm O_2 ; < 1 ppm H_2O). Experimental procedures were optimized for machine readability using SynCheck as shown in Figure S1.

For the conversion reaction of copper compounds, 1 g of the precursor salt (CuCl , CuBr , CuCl_2 , CuBr_2 , CuI , CuF_2 , CuO , or Cu_2O) was dispersed in hexane (10 mL). Next, *n*-butyllithium (1.25 \times stoichiometric excess) was added dropwise to the precursor dispersion, and the resulting mixture was then stirred at room temperature for 24 h. The obtained powder of nanocomposites was separated by filtration, washed with hexane (10 mL), and dried under an argon atmosphere. For annealing experiments, powders were sealed in borosilicate ampoules under vacuum. Each sample was then annealed at a constant temperature of 100–300 °C for 1 h and then quenched to room temperature.

Mg-doped copper oxide was synthesized in two steps.¹⁹ In a first step, $\text{CuSO}_4 \cdot 5\text{H}_2\text{O}$ and $\text{Mg}(\text{NO}_3)_2$ (20:1 molar excess) were dissolved in water. Second, the precursor solution was mixed (dropwise) with a NaOH solution at 80 °C for 2 h under continuous stirring, resulting in the immediate

formation of a black precipitate. The reaction product was then collected through centrifugation (4000 rpm, 10 min) and washed with DI water and absolute ethanol. The resulting product was heated at 70 °C for 12 h in a drying cabinet, producing a black powder. The same procedure is applied to synthesize pure CuO without adding the Mg dopant solution.

Material Characterization. Scanning electron microscopy (SEM) images and energy-dispersive X-ray (EDX) spectra were acquired with a Zeiss Sigma 500 SEM. Due to the sensitivity of the nanocomposite to oxygen and moisture, all X-ray diffraction (XRD) patterns were acquired using a circular sample holder under the protection of Kapton tape. A powder diffractometer (Bruker D2 Phaser) was used for collecting the XRD patterns using Cu $K\alpha$ radiation ($\lambda = 1.5418$ Å, 40 kV, 40 mA) in a 2θ range from 10 to 80° at a scan rate of 0.01 °/s. The Inorganic Crystal Structure Database (ICSD) was used to identify the phases in the nanocomposites.

TEM images are obtained on a ThermoFisher Talos 200X system. A copper-coated TEM grid is used to load nanocomposite powder, which is loaded into the sample holder in an argon glovebox. Then, the holder is transferred and inserted under argon protection. Images and lattice parameters are analyzed using the Gatan Micrograph software.

Rietveld refinements were performed in TOPAS (Version 6, Bruker AXS)²⁰ to determine the microstructural properties of the Cu and salt phases. A fundamental parameter approach^{21,22} was used to model the instrument profile, incorporating a 0.6 mm divergence slit, 20 mm sample length, 250 mm beam path length, and 2.5° Soller slits. Sample displacements were refined for each pattern to account for systematic shifts in peak positions resulting from the difference in sample height on the flat plate holder. Preferred orientation (e.g., oversampling of particular *hkl* reflections) was accounted for using the March–Dollase factor to correct misfits to peak intensities and is reported in Table S1. In nearly all nanocomposites (except CuI, CuBr, and CuCl), the Cu phase demonstrated preferred orientation in the $\langle 111 \rangle$ direction, with a refined March–Dollase factor indicating that the crystallites are longer in that direction. Note that this preferred orientation cannot trivially occur for the nanoscale grains and suggests that there is a topotactic relationship between the salt in the nanocomposite reaction product and that of the copper reaction precursors, which typically were used in the form of micron-scale particles. For the LiBr and LiCl salt phases produced from CuBr_2 , CuCl , or CuCl_2 , a preferred orientation term was refined in the $\langle 111 \rangle$ direction to account for systematic underfitting of intensity in that direction and overfitting of intensity in other directions. The results indicate that salt crystallites are less prevalent in the $\langle 111 \rangle$ direction for CuBr_2 - and CuCl -based nanocomposites, while the salt from a CuCl_2 precursor is more prevalent in the $\langle 111 \rangle$ direction.

The microstructure (e.g., crystallite size and lattice strain) was determined for each phase by fitting peak shapes using the Double–Voigt approach as this allows for the effective deconvolution of the contributions from size broadening (varies as $1/\cos \theta$) and strain broadening (varies as $\tan \theta$).^{23,24} Generally, only a Lorentzian size broadening term was needed to describe Cu peak shapes. For chloride and bromide salt phases, both size and strain broadening terms were needed to account for broadening, while only size broadening models were needed for the iodide, fluoride, and various copper oxide-based nanocomposites.

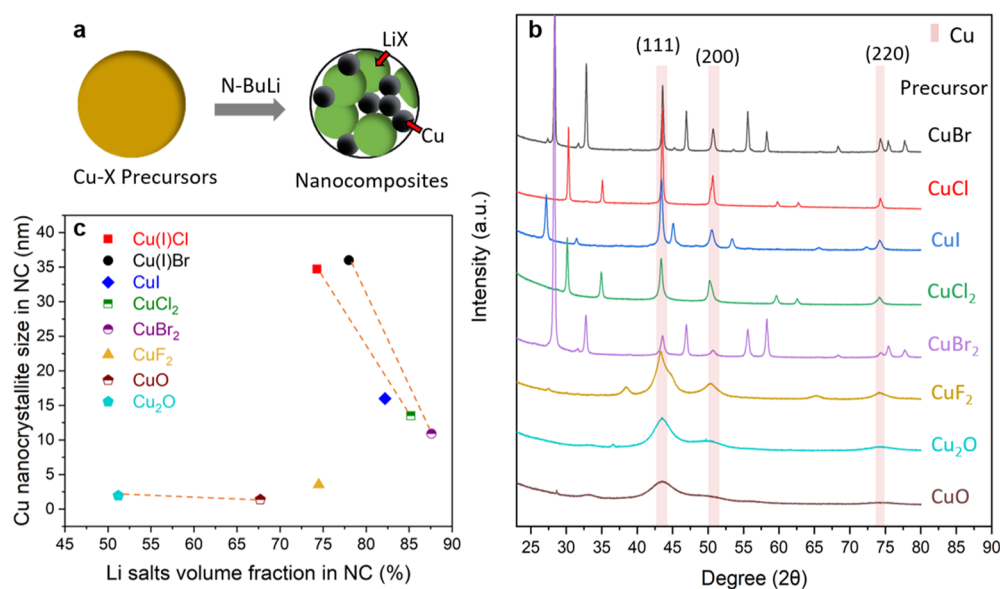


Figure 1. (a) Illustration of the nanocomposite preparation through the conversion reaction. (b) XRD patterns of Cu/Li salt nanocomposites. Precursors are labeled on the right of each pattern. (c) Relationship between Cu nanocrystallite size in the NC and the volume fractions of the corresponding Li salts. Precursors with a common anion are connected by a dashed line.

Crystallite sizes are reported (Table S2) as volume-weighted crystallite sizes (L_{vol}) determined through an integral breadth (IB) method that is approximately independent of the shape factor, K , that is often approximated as 0.89–1 in the Scherrer equation. Since particle shapes and size distributions are typically unknown, IB methods are more robust for microstructure determination. The volume-weighted size (L_{vol} in nm) is calculated as shown from the equation below, where β_{IB} is defined as the width of a rectangle with the same height and area as the line profile, obtained by dividing the peak area by the maximum peak height.

$$L_{\text{vol}} = \frac{\lambda}{\beta_{\text{IB}} \cdot \cos \theta}$$

Lattice strain values (Table S2) represent the maximum displacement of the lattice or the maximum strain moment (ϵ_0). In our prior work on size–strain analysis for CRS-derived metal/salt nanocomposites,¹⁸ it was found that the salt lattice strain is likely due to the chemical substitution of metal ions in the salt phase that (1) produce vacancies to maintain charge neutrality and (2) cause lattice expansion or contraction as a result of differences in the ionic radii of Li^+ and $\text{M}^{\text{X}+}$ ($\text{M} = \text{Fe}, \text{Co}, \text{and Cu}; \text{X} = 1, 2, \text{and } 3$). Due to the systematic decrease of strain in the bromide and chloride salts after thermal annealing, we attribute strain in the salt phase of the Cu-NP nanocomposites to the same mechanism. The equation for calculating the maximum strain moment is given below

$$\epsilon_0 = \frac{\Delta d}{d} = \frac{\beta_{\text{FWHM}}}{4 \tan \theta}$$

First-Principles Calculations. First-principles density functional theory (DFT) calculations were carried out using the Vienna Ab Initio Simulation Package (VASP).^{25,26} The projector-augmented wave potential was employed for the treatment of the electron–ion interactions,²⁷ and the generalized gradient approximation parameterized by Perdew–Burke–Ernzerhof was used for the electron exchange–correlation functional.²⁸ The default maximum cut-off energy

from the potential files was used for expanding the plane-wave basis set. The k -points grid with a separation of 0.04 \AA^{-1} centered at the Γ -point was automatically set for the calculations. The structural relaxation was performed until all components of the residual forces on the atoms became less than 0.05 eV \AA^{-1} and the convergence tolerance for the self-consistent-field iteration was set to 10^{-4} eV . Cu diffusion energy barriers were calculated using the climbing image nudged elastic band (NEB) method.²⁹ In the NEB calculations, the starting and ending structures were fully relaxed, and the intermediate structures were linearly interpolated.

RESULTS AND DISCUSSION

To study the precursor anion effects on the Cu microstructure evolution during the CRS of nanoporous Cu, we selected eight different Cu precursor compounds [Cu(I)Cl, CuCl₂, Cu(I)Br, CuBr₂, CuF₂, Cu(I)I, CuO, and Cu₂O] and converted them under identical experimental conditions (Figure 1a). Powder XRD patterns of the nanocomposites (Figure 1b) indicated complete consumption of the precursor, suggesting that the conversion reaction was complete. All of the halide precursors clearly exhibited two main phases (Cu metal and Li salt, peak assignments shown in Figure S2) after the conversion step. The very broad peaks indicate that metallic Cu within the nanocomposite has primary particles with nanoscale dimensions. The lithium salts in the nanocomposites were then removed by dissolution in methanol or water, allowing the morphologies of NP-Cu synthesized from different precursors to be compared (Figure S3). It is evident that the anions can greatly affect the microstructure evolution during the conversion reaction, producing NP-Cu with very different pore dimensions.

The Rietveld refinement was performed to quantify the microstructure of both the copper and salt phases in nanocomposites from the diffraction data. Details of the refinement methods, examples of the fits (Figures S4–S11),

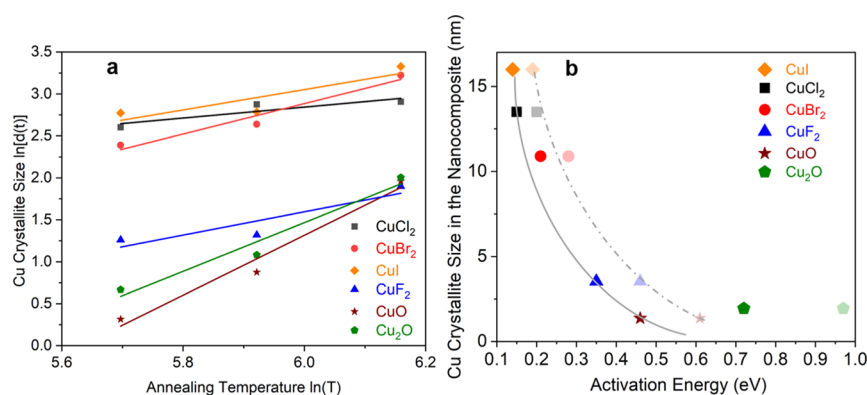


Figure 2. (a) Dependence of Cu nanocrystallite size (in the nanocomposite) and annealing temperature for all the precursors. (b) Relationship between the average crystallite size and activation energy calculated from eq 1. Light symbol dots refer to activation energies calculated assuming a surface diffusion mechanism ($n = 4$), while normal color symbols were calculated assuming a bulk diffusion mechanism ($n = 3$).

and tabulated crystallographic info (Tables S1 and S2) are provided in the Supporting Information.

Influence of Volume Fraction. Previous studies¹⁴ suggested that lithium salts could physically hinder the metal diffusion during the reaction, which intuitively would suggest that a high volume of lithium salts would promote the formation of finer microstructures. Based on the theoretical reaction stoichiometry, we calculated the volume fraction of Li salts in the nanocomposites. The results and details of calculation are provided in the Supporting Information (Table S3). By looking at the relationship between volume fraction and Cu nanocrystallite sizes, we found that the hindering effect of Li salts is indeed true when the anions are the same. For example, the nanocomposite formed from CuCl₂ which is 85% LiCl by volume resulted in a smaller Cu size (13.5 nm) compared with the CuCl case (34.7 nm), for which the LiCl volume fraction is 74% (Figure 1c). However, such trends do not hold when comparing salts containing different anions. For instance, the use of a CuF₂ precursor leads to the finest Cu size (3.5 nm) among the halide precursors despite having the smallest salt volume fraction. The microstructure of CuCl₂ and CuF₂ is further examined by transmission electron microscopy (TEM) (Figures S12 and S13). Both of them show a bicontinuous nanocomposite structure with uniform elemental distribution analyzed by EDX spectroscopy. The crystal sizes of Cu are 9–15 and 3–6 nm when CuCl₂ and CuF₂ are used as the precursors, respectively. This result is consistent with the Rietveld refinement. Hence, the salt volume fractions are not the primary factor controlling the Cu-NP size.

Influence of Diffusion Barrier. Since the particle size was strongly dependent on the choice of the starting material, we hypothesized that the diffusion barrier for Cu may play an important role. Similar justifications have previously been made for dealloying reactions.^{18,30} To measure the activation energy for Cu diffusion, we employed a series of thermal annealing experiments.¹⁸ The nanocomposites were isothermally annealed at 100, 200, or 300 °C for 1 h, with the resulting diffraction patterns and their fits shown in Figures S4–S11. The crystallite size obtained from diffraction data was found to systematically vary with the annealing temperature. Specifically, it was observed that there is a linear relationship between $\ln[d(t)]$ and $\ln(T)$, where $d(t)$ is the size of Cu and T is the annealing temperature (Figure 2a), consistent with general models for coarsening that have been previously

derived.³¹ Cu(I)Cl and Cu(I)Br cases were not evaluated because of their relatively large crystallite size after thermal annealing, which reduces the sensitivity of diffraction methods to changes in particle size.^{32–34} The activation energy (E) required for diffusion can be calculated based on the equation^{35–37}

$$[d(t)]^n = k_0 t \exp\left(\frac{-E}{RT}\right) \quad (1)$$

where $d(t)$ is the average crystallite size of metals at different annealing time t , k_0 is a constant, R is the gas constant, and T is the annealing temperature. For the power n in the power law, it has been reported that values of 3 and 4 correspond to cases where the diffusion and coarsening are dominated by bulk diffusion and surface diffusion, respectively.³⁶ Since the diffusion mechanism is not known a priori, the activation energy for each nanocomposite was separately evaluated for each n value (Figure S14). The inferred activation energy for $n = 4$ was about 4/3 the value for $n = 3$, the behavior which is expected to be a universal result originating from the two different mathematical functions. It was found that there is a well-defined inverse correlation between the activation energy and the average Cu crystallite size within the nanocomposites, as shown in Figure 2b. The strongly linear relationship between the energy barrier for diffusion and the identity of anions indicates that the fundamental mechanism by which anions control the size of NP-Cu is related to transport through an anion-containing phase, suggesting that the previously observed relationship between self-diffusion coefficients in metals and the particle size in the nanoporous metal frameworks produced through CRS reflects correlation rather than causation.¹⁸

Investigate the Diffusion Pathways by DFT Calculation. The thermal annealing results revealed the importance of the energy barrier for diffusion in controlling the size and porosity of nanoporous Cu. However, it was not possible to resolve whether these barriers are associated with surface or bulk diffusion pathways due to the similar fit quality of both of these models. To more directly resolve the nature of the activation energy for Cu atom diffusion, we investigated surface diffusion and bulk diffusion of Cu atoms in the lithium halide salts using NEB methods based on the first-principles DFT calculations.²⁹ The similar halide crystal structures make it more straightforward and robust to investigate trends. For LiX ($X = \text{F, Cl, Br, and I}$), the electrically neutral (001)

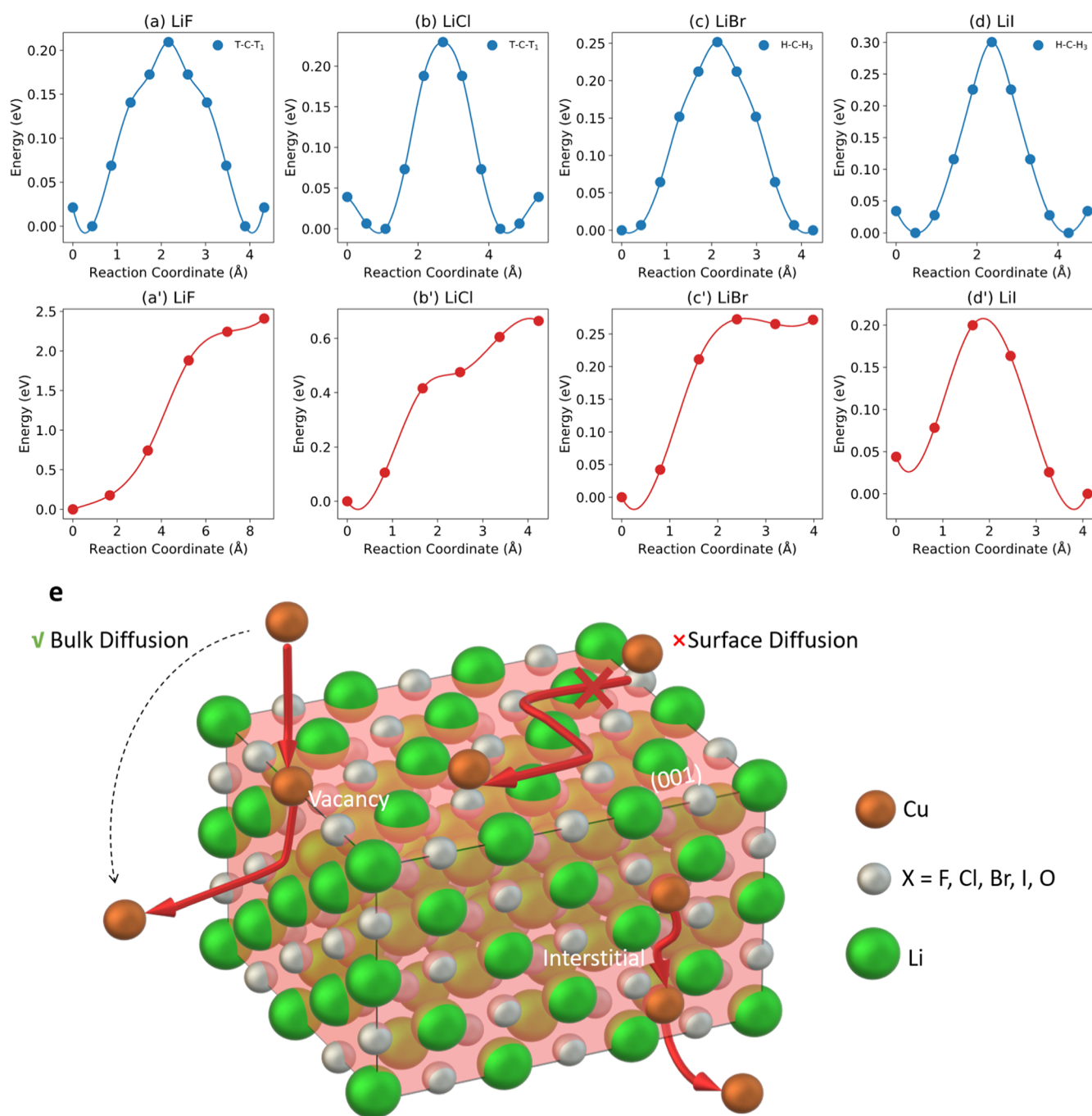


Figure 3. Calculated diffusion barriers of Cu ions on the (001) surface (a–d) and the corresponding bulk diffusion barriers (a'–d') for the cubic (a,a') LiF, (b,b') LiCl, (c,c') LiBr, and (d,d') LiI. (e) Illustration of Cu atom diffusion during the conversion reaction or high-temperature sintering. Cu mainly diffuses through the defects rather than the surface of Li salts.

surfaces are known to be energetically more stable than the polar (111) surfaces^{38,39} and thus were selected to model Cu surface diffusion (Figure S15a). According to the surface symmetry, we modeled four possible sites for a single Cu atom adsorption, including a top (T) site directly above the X atom, a bridge (B) site on the middle of the surface X–Li bond, a cap (C) site directly above the Li atom, and a hollow (H) site above the center of the square formed by four X–Li bonds. The equivalent sites for T and H are labeled as T₁ and H₁. The energetic preference of the Cu adsorption on the four possible sites were determined via a comparison of the relative total energies for the LiX (001) slab models with Cu adsorption, as

shown in the Table S4 in the Supporting Information. Our calculations show that the energetically most favorable Cu adsorption site is T for LiF, B for LiCl, and H for LiBr and LiI, while the most unfavorable site is C for all the considered lithium salt compounds. Accordingly, we modeled the diffusion pathways T–C–T₁ for LiF and LiCl and H–C–H₁ for LiBr and LiI. The calculated surface diffusion energy barriers are around 0.21 eV for LiF, 0.23 eV for LiCl, 0.25 eV for LiBr, and 0.30 eV for LiI, as shown in Figure 3a–d. Note that the trend for surface diffusion activation energies is LiF < LiBr < LiCl < LiI, exactly opposite of what was observed experimentally.

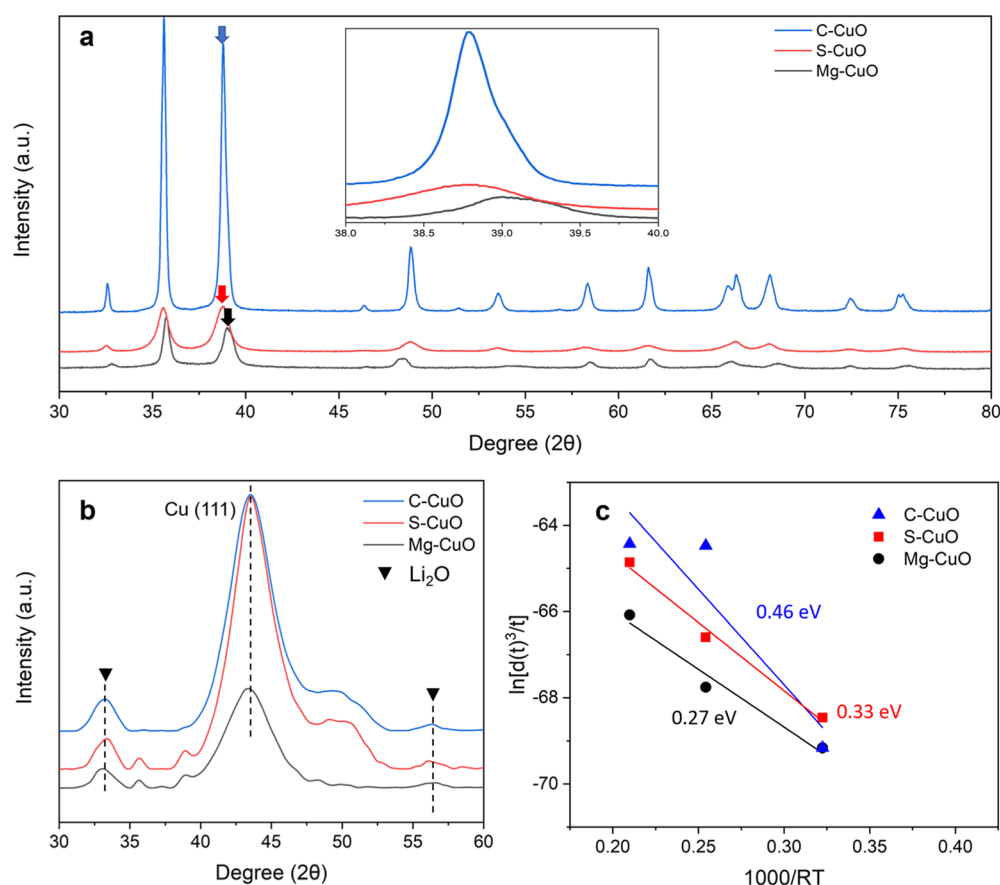


Figure 4. Effects of MgO doping of CuO on (a) XRD patterns of the precursor phases, (b) XRD patterns of the nanocomposite reaction product, and (c) activation energies inferred from ex situ coarsening studies.

Next, the possibility of a diffusion mechanism involving transport through the bulk of the lithium salts was examined. This appears to be the case since we have observed a correlation between the activation energy (obtained assuming $n = 3$ in eq 1) and the melting point of a corresponding lithium salt (Figure S16). Here, the melting point is used as a proxy for the concentration of defects. In general, the lower the melting point, the more favorable the point defect formation.^{40,41} During the conversion reaction or high-temperature sintering, native point defects are generated in the lattice of lithium salt crystals. More defects in the lithium salt matrix can promote the diffusion and growth of Cu. Indeed, it has been found that the defect formation energies always follow the sequence as $\text{LiF} > \text{LiCl} > \text{LiBr} > \text{LiI}$ for both vacancy and interstitial defects, consistent with the trend of Cu crystallite sizes we have obtained.^{42,43} To further prove this, DFT was used to model the possible bulk diffusion pathway for the Cu ions, see its schematic illustration of the diffusion path in Figure S15b. The calculated energy barriers of Cu bulk diffusion are 2.6 eV for LiF, 0.66 eV for LiCl, 0.26 eV for LiBr, and 0.16 eV for LiI, as shown in Figure 3a'–d'. This indicates that the Cu bulk diffusion is more difficult in the order $\text{LiI} < \text{LiBr} < \text{LiCl} < \text{LiF}$, which are mainly attributed to the different lattice size due to the different atomic radius of halogen ions. This trend is also consistent with our experimental observations. We note that the nanostructured lithium halides are likely rich in defects which would impact the energy barriers for diffusion. However, the trends we observed in the halide series strongly suggest a bulk, rather than a surface-mediated diffusion process is at play.

The concept for this Cu atom diffusion pathway is illustrated in Figure 3e.

Probing the Effect of Defects with Doping. A dopant was introduced into the precursor compound to further validate that the diffusion of Cu atoms mainly takes place in the defects of bulk lithium salt phases. If the primary diffusion processes responsible for the growth in particle size occur in the Cu metal phase, then the growth rate should not be affected by dopants, whereas the observation of dopant effects provides strong evidence that growth occurs through diffusion pathways external to Cu metal particles. We chose magnesium (Mg) as a dopant because the electrochemical potential of Mg^{2+}/Mg (-2.38 V) is lower than -2.05 V, the potential of *n*-butyllithium, preventing the reduction of Mg^{2+} .¹⁴ This choice also benefits from the similar radius of Mg^{2+} (72 pm) and Cu^{2+} (73 pm). Many methods have been established to dope Mg elements into CuO.^{19,44,45} Using previously reported procedures, we synthesized CuO doped with Mg (Mg–CuO) by a co-precipitation method. A comparison between the XRD patterns of Mg–CuO and two pure CuO samples is shown in Figure 4a, where S–CuO represents the CuO synthesized by the same procedures as Mg–CuO without the dopant, while C–CuO is a bulk crystal obtained commercially. All materials match the CuO monoclinic crystal structure according to the ICSD database. The broadening of peaks for Mg–CuO and S–CuO indicates the formation of nanoscale particle sizes. The peak shift at 2θ values of 35.6, 38.8, and 48.8° indicates that Mg was successfully doped into CuO^{19,44,45} and is supported by EDX mapping (Figure S17a). Figure 4b shows

the XRD patterns of the nanocomposites formed after conversion through the reaction with *n*-butyllithium. A slightly left shift at $2\theta = \sim 33.6^\circ$, which corresponds to the peak of the (111) plane of Li_2O , indicates that the Mg dopant is inherited by Li_2O in the nanocomposite. The EDX result of the nanocomposite in Figure S17b also confirms the presence of Mg after conversion. Doping Li_2O with Mg is expected to create more vacancies in the Li_2O phase, which is expected to increase the mobility and result in larger crystallite sizes. The activation energies were also calculated and shown in Figure 4c, which were fully consistent with our hypothesis. The nanocomposite via Mg–CuO has the lowest energy (0.27 eV) for Cu diffusion among the three types of CuO. Based on these observations, we conclude that the diffusivity of Cu atoms through defects of Li salts determines the specific dimension of Cu in the intermediates.

CONCLUSIONS

By conducting conversion reactions on Cu compounds with various anions, we have demonstrated that different anions can effectively change the Cu crystallite dimensions within the nanocomposites and consequently determine the microstructure size in the final NP-Cu. A dilute Cu concentration will reduce the resultant size, but this volumetric effect only holds true for Cu compounds with identical anions. For different anions, we have found that the Cu size directly correlates with the diffusion energy barrier, which was estimated by measuring the size of Cu undergoing thermal annealing. We identified that Cu appears to coarsen by diffusing through the defects in the bulk lithium salt phases rather than through the Cu/lithium salt interface. This is confirmed both by the energy barrier trends in the halide series using DFT calculations and by increasing the defect concentration through doping, which led to an increase in Cu size. Our findings thus provide insights into the fundamental diffusion process in nanocomposites and offer anions and dopants as practical toolkits to control the Cu sizes.

ASSOCIATED CONTENT

Supporting Information

The Supporting Information is available free of charge at <https://pubs.acs.org/doi/10.1021/acs.jpcc.2c03544>.

Experimental procedures; XRD patterns of nanocomposites at different annealing temperatures; SEM images of pure nanoporous Cu; Rietveld refinement of XRD; TEM of the representative nanocomposites; evaluation of activation energy; diffusion pathway schematic illustration; correlation between activation energy and melting point of Li salts; EDX elemental mapping of doped CuO and its nanocomposite; tabulated crystallographic info; reaction equation and volume fraction calculations; and Cu adsorption energy comparison on the (001) slab (PDF)

AUTHOR INFORMATION

Corresponding Author

Ping Liu – *Materials Science and Engineering Program and Department of Nanoengineering, University of California San Diego, La Jolla, California 92093, United States*; orcid.org/0000-0002-1488-1668; Email: pliu@eng.ucsd.edu

Authors

Shijie Feng – *Materials Science and Engineering Program, University of California San Diego, La Jolla, California 92093, United States*; orcid.org/0000-0001-5797-8542

Victoria Petrova – *Materials Science and Engineering Program, University of California San Diego, La Jolla, California 92093, United States*

Adam A. Corrao – *Department of Chemistry, Stony Brook University, Stony Brook, New York 11794, United States; Division of Chemistry, Brookhaven National Laboratory, Upton, New York 11973, United States*; orcid.org/0000-0001-6111-8959

Shen Wang – *Department of Nanoengineering, University of California San Diego, La Jolla, California 92093, United States*

Kesong Yang – *Materials Science and Engineering Program and Department of Nanoengineering, University of California San Diego, La Jolla, California 92093, United States*; orcid.org/0000-0002-9691-0636

Peter G. Khalifah – *Department of Chemistry, Stony Brook University, Stony Brook, New York 11794, United States; Division of Chemistry, Brookhaven National Laboratory, Upton, New York 11973, United States*; orcid.org/0000-0002-2216-0377

Complete contact information is available at: <https://pubs.acs.org/doi/10.1021/acs.jpcc.2c03544>

Author Contributions

S.F. synthesized the samples and performed and analyzed the lab XRD data with guidance from P.L. V.P. assisted in the collection of SEM data. S.W. performed TEM. A.C. carried out the XRD data analysis by the Rietveld refinement with the guidance from P.G.K. K.Y. carried out DFT computational work. A.C., P.G.K., and P.L. assisted in understanding the data and discussing the main diffusion mechanisms behind various systems. The manuscript was primarily written by S.F. and P.L. with contributions from all the co-authors.

Notes

The authors declare no competing financial interest.

ACKNOWLEDGMENTS

This work was supported as part of GENESIS: A Next Generation Synthesis Center, an Energy Frontier Research Center funded by the U.S. Department of Energy, Office of Science, Basic Energy Sciences under award number DE-SC0019212. This work was performed in part at the San Diego Nanotechnology Infrastructure (SDNI) of UCSD, a member of the National Nanotechnology Coordinated Infrastructure (NNCI), which is supported by the National Science Foundation (grant ECCS-1542148). Partial support for AAC was provided by an NRT QuADS Fellowship (Quantitative Analysis of Dynamic Structures) under NSF DGE-1922639. The computational work used the Extreme Science and Engineering Discovery Environment (XSEDE), which is supported by the National Science Foundation (grant no. ACI-1548562).

REFERENCES

(1) Koya, A. N.; Zhu, X.; Ohannesian, N.; Yanik, A. A.; Alabastri, A.; Proietti Zaccaria, R.; Krahn, R.; Shih, W. C.; Garoli, D. Nanoporous Metals: From Plasmonic Properties to Applications in Enhanced Spectroscopy and Photocatalysis. *ACS Nano* **2021**, *15*, 6038–6060.

- (2) Chen, L.-Y.; Yu, J.-S.; Fujita, T.; Chen, M.-W. Nanoporous Copper with Tunable Nanoporosity for SERS Applications. *Adv. Funct. Mater.* **2009**, *19*, 1221–1226.
- (3) Song, R.; Zhang, L.; Zhu, F.; Li, W.; Fu, Z.; Chen, B.; Chen, M.; Zeng, H.; Pan, D. Hierarchical Nanoporous Copper Fabricated by One-Step Dealloying Toward Ultrasensitive Surface-Enhanced Raman Sensing. *Adv. Mater. Interfac.* **2018**, *5*, 1800332.
- (4) Xie, H.; Wang, T.; Liang, J.; Li, Q.; Sun, S. Cu-based nanocatalysts for electrochemical reduction of CO₂. *Nano Today* **2018**, *21*, 41–54.
- (5) Yang, K. D.; Ko, W. R.; Lee, J. H.; Kim, S. J.; Lee, H.; Lee, M. H.; Nam, K. T. Morphology-Directed Selective Production of Ethylene or Ethane from CO₂ on a Cu Mesopore Electrode. *Angew. Chem., Int. Ed. Engl.* **2017**, *56*, 796–800.
- (6) Sen, S.; Liu, D.; Palmore, G. T. R. Electrochemical Reduction of CO₂ at Copper Nanofoams. *ACS Catal.* **2014**, *4*, 3091–3095.
- (7) Han, G.; Um, J. H.; Park, H.; Hong, K.; Yoon, W.-S.; Choe, H. Hierarchically structured nanoporous copper for use as lithium-ion battery anode. *Scr. Mater.* **2019**, *163*, 9–13.
- (8) Bai, Q.; Zhang, C.; Tan, F.; Wu, F.; Zhang, Z. Nanoporous copper as an inexpensive electrochemical actuator responsive to sub-volt voltages. *Electrochem. Commun.* **2021**, *124*, 106940.
- (9) Mohan, K.; Shahane, N.; Liu, R.; Smet, V.; Antoniou, A. A Review of Nanoporous Metals in Interconnects. *Jom* **2018**, *70*, 2192–2204.
- (10) Sun, S.; Guo, Q.; Chen, H.; Li, M.; Wang, C. Solderless bonding with nanoporous copper as interlayer for high-temperature applications. *Microelectron. Reliab.* **2018**, *80*, 198–204.
- (11) Koga, S.; Nishikawa, H.; Saito, M.; Mizuno, J. Fabrication of Nanoporous Cu Sheet and Application to Bonding for High-Temperature Applications. *J. Electron. Mater.* **2020**, *49*, 2151–2158.
- (12) Wang, N.; Pan, Y.; Wu, S.; Zhang, E.; Dai, W. Fabrication of nanoporous copper with tunable ligaments and promising sonocatalytic performance by dealloying Cu–Y metallic glasses. *RSC Adv.* **2017**, *7*, 43255–43265.
- (13) Chen, G.; Pan, Y.; Lu, T.; Wang, N.; Li, X. Highly catalytic performance of nanoporous copper for electro-oxidation of methanol in alkaline media. *Mater. Chem. Phys.* **2018**, *218*, 108–115.
- (14) Coaty, C.; Zhou, H.; Liu, H.; Liu, P. A Scalable Synthesis Pathway to Nanoporous Metal Structures. *ACS Nano* **2018**, *12*, 432–440.
- (15) McCue, I.; Benn, E.; Gaskey, B.; Erlebacher, J. Dealloying and Dealloyed Materials. *Annu. Rev. Mater. Res.* **2016**, *46*, 263–286.
- (16) Ignaczak, A.; Gomes, J. A. N. F. Interaction of Halide Ions with Copper: the DFT approach. *Chem. Phys. Lett.* **1996**, *257*, 609–615.
- (17) Kuznetso, An. M. Ab Initio Quantum-chemical Studies of Halogen Atoms and Halogenide Ions Chemisorbed on a Cu(III) Surface. *Electrochim. Acta* **1995**, *40*, 2483–2485.
- (18) Coaty, C. M.; Corrao, A. A.; Petrova, V.; Khalifah, P. G.; Liu, P. Morphological Tuning of Nanoporous Metals Prepared with Conversion Reaction Synthesis via Thermal Annealing. *J. Phys. Chem. C* **2019**, *123*, 17873–17883.
- (19) Din, S. U.; Sajid, M.; Imran, M.; Iqbal, J.; Shah, B. A.; Azeem ullah, M.; Shah, S. One step facile synthesis, characterization and antimicrobial properties of Mg-doped CuO nanostructures. *Mater. Res. Express* **2019**, *6*, 085022.
- (20) Coelho, A. A. TOPAS and TOPAS-Academic: An Optimization Program Integrating Computer Algebra and Crystallographic Objects Written in C++. *An. J. Appl. Crystallogr.* **2018**, *51*, 210–218.
- (21) Cheary, R. W.; Coelho, A. A. A fundamental parameters approach to X-ray line-profile fitting. *J. Appl. Crystallogr.* **1992**, *25*, 109–121.
- (22) Cheary, R. W.; Coelho, A. A.; Cline, J. P. Fundamental Parameters Line Profile Fitting in Laboratory Diffractometers. *J. Res. Natl. Inst. Stand Technol.* **2004**, *109*, 1–25.
- (23) Balzar, D.; Ledbetter, H. Voigt-function modeling in Fourier analysis of size- and strain-broadened X-ray diffraction peaks. *J. Appl. Crystallogr.* **1993**, *26*, 97–103.
- (24) Balzar, D.; Audebrand, N.; Daymond, M. R.; Fitch, A.; Hewat, A.; Langford, J. I.; Le Bail, A.; Louër, D.; Masson, O.; McCowan, C. N.; et al. Size–strain line-broadening analysis of the ceria round-robin sample. *J. Appl. Crystallogr.* **2004**, *37*, 911–924.
- (25) Kresse, G.; Furthmüller, J. Efficiency of ab-initio total energy calculations for metals and semiconductors using a plane-wave basis set. *Comput. Mater. Sci.* **1996**, *6*, 15–50.
- (26) Kresse, G.; Furthmüller, J. Efficient iterative schemes for ab initio total-energy calculations using a plane-wave basis set. *Phys. Rev. B: Condens. Matter Mater. Phys.* **1996**, *54*, 11169–11186.
- (27) Blöchl, P. E. Projector augmented-wave method. *Phys. Rev. B: Condens. Matter Mater. Phys.* **1994**, *50*, 17953–17979.
- (28) Perdew, J. P.; Burke, K.; Ernzerhof, M. Generalized Gradient Approximation Made Simple. *Phys. Rev. Lett.* **1996**, *77*, 3865–3868.
- (29) Henkelman, G.; Uberuaga, B. P.; Jónsson, H. A climbing image nudged elastic band method for finding saddle points and minimum energy paths. *J. Chem. Phys.* **2000**, *113*, 9901.
- (30) Juarez, T.; Biener, J.; Weissmüller, J.; Hodge, A. M. Nanoporous Metals with Structural Hierarchy: A Review. *Adv. Eng. Mater.* **2017**, *19*, 1700389.
- (31) Qian, L. H.; Chen, M. W. Ultrafine nanoporous gold by low-temperature dealloying and kinetics of nanopore formation. *Appl. Phys. Lett.* **2007**, *91*, 083105.
- (32) He, K.; Chen, N.; Wang, C.; Wei, L.; Chen, J. Method for Determining Crystal Grain Size by X-Ray Diffraction. *Cryst. Res. Technol.* **2018**, *53*, 1700157.
- (33) Holder, C. F.; Schaak, R. E. Tutorial on Powder X-ray Diffraction for Characterizing Nanoscale Materials. *ACS Nano* **2019**, *13*, 7359–7365.
- (34) Rabiei, M.; Palevicius, A.; Monshi, A.; Nasiri, S.; Vilkauskas, A.; Janusas, G. Comparing Methods for Calculating Nano Crystal Size of Natural Hydroxyapatite Using X-Ray Diffraction. *Nanomaterials* **2020**, *10*, 1627.
- (35) Erlebacher, J. Mechanism of coarsening and bubble formation in high-genus nanoporous metals. *Phys. Rev. Lett.* **2011**, *106*, 225504.
- (36) Chen-Wiegart, Y.-c. K.; Wang, S.; Chu, Y. S.; Liu, W.; McNulty, I.; Voorhees, P. W.; Dunand, D. C. Structural evolution of nanoporous gold during thermal coarsening. *Acta Mater.* **2012**, *60*, 4972–4981.
- (37) Liu, W.; Cheng, P.; Yan, J.; Li, N.; Shi, S.; Zhang, S. Temperature-induced surface reconstruction and interface structure evolution on ligament of nanoporous copper. *Sci. Rep.* **2018**, *8*, 447.
- (38) Hebenstreit, W.; Schmid, M.; Redinger, J.; Podloucky, R.; Varga, P. Bulk terminated NaCl(111) on aluminum: a polar surface of an ionic crystal? *Phys. Rev. Lett.* **2000**, *85*, 5376–5379.
- (39) Liu, Z.; Qi, Y.; Lin, Y. X.; Chen, L.; Lu, P.; Chen, L. Q. Interfacial Study on Solid Electrolyte Interphase at Li Metal Anode: Implication for Li Dendrite Growth. *J. Electrochem. Soc.* **2016**, *163*, A592–A598.
- (40) Haven, Y. The ionic conductivity of Li-halide crystals. *Recl. Trav. Chim. Pays-Bas* **1950**, *69*, 1471.
- (41) Ksiazek, K.; Górecki, T. Changes in the heat capacity of alkali halides on passing through the melting point and the vacancy model of melting. *J. Mater. Sci. Lett.* **2001**, *20*, 1623–1625.
- (42) Banhatti, R. D.; Murti, Y. V. G. S. Majority and minority intrinsic defects in lithium and sodium halides. *Bull. Mater. Sci.* **1997**, *20*, 451–454.
- (43) Rowell, D. K.; Sangster, M. J. L. Calculations of Intrinsic Defect Energies in the Alkali Halides. *J. Phys. C Solid State Phys.* **1981**, *14*, 2909.
- (44) Varghese, R.; Joy Prabu, H.; Johnson, I. Synthesis and Characterization of Mg Doped CuO Nano Particles by Quick Precipitation Method. *Materials, Energy and Environment Engineering*; Springer, 2017; pp 159–165.
- (45) Lv, Y.; Li, L.; Yin, P.; Lei, T. Synthesis and evaluation of the structural and antibacterial properties of doped copper oxide. *Dalton Trans.* **2020**, *49*, 4699–4709.